scientific reports

Check for updates

OPEN

Isolation of adipose stromal cells from blood using a two-step microfluidic platform ASCfinder

Mohammad-H. Baz[1,2]✉, Marion Valette[1], Mireille André[2], Audrey Varin[2], Emmanuelle Trevisiol[1,3], Coralie Sengenès[2] & Anne-Marie Gue[1]✉

Mesenchymal stromal cells (MSCs) hold significant promise for their therapeutic potential and their possible role as disease biomarkers. While evidence suggests the presence of circulating Adipose-derived MSC (ASC) in peripheral blood (PB), isolating them is particularly challenging due to their low abundance, size variability, and incomplete characterization of their native immunophenotype in PB. Consequently, the relationship between ASC frequency in blood and various physiological or pathological conditions has been underexplored. In this study, we introduce ASC-Finder, a label-free isolation method specifically designed for adipose stromal cells (ASCs), a key MSC population. ASC-Finder integrates two independent modules: a size-dependent hydrodynamic filtration unit for sorting erythrocytes directly from PB and a negative enrichment module based on immunological markers to deplete remaining leukocytes. The device enabled removal of 99.98% of erythrocytes while achieving high recovery rates of spiked ASCs (> 81%) at rare-event concentrations (< 100 ASC/mL blood). Remarkably, ASC-Finder operates without clogging, even after multiple runs with donor blood samples. Crucially, our method bypasses the need for harsh lysis, centrifugation, or dilution buffers, preserving both cell integrity and phenotype—key factors for the discovery of novel cellular events. This work represents a significant advancement in the direct enrichment of circulating ASCs from whole PB without cell lysis, offering a crucial step toward investigating the characterization and role of blood-circulating ASCs.

Mesenchymal stromal cells (MSCs) are multipotent stromal cells that can differentiate into adipocytes, osteocytes, and chondrocytes. Found in the bone marrow and other tissues, MSCs exhibit significant immunomodulatory properties that support tissue repair and immune regulation. Adipose-derived stromal cells (ASCs), identified in 2002 by Zuk et al., are considered a type of MSCs derived from adipose tissue (AT)[1]. Like their bone marrow counterparts (BM-MSCs), ASCs are known for their immunomodulatory and anti-inflammatory properties[2]. They have been thoroughly investigated for their therapeutic potential in various medical conditions, such as autoimmune diseases, inflammatory disorders, tissue injuries and more recently as immediate therapy for severe pneumonia in Covid-19 patients[3–5].

ASCs reside within AT and are viewed as tissue-resident cells. However, increasing evidence shows that ASCs are mobile and can migrate to distant tissues in response to various physiological and pathophysiological stresses. In this context, we have demonstrated that ASCs can relocate from subcutaneous AT to sites of inflammation or injury. Our previous work has shown in mice that metabolic stresses (high fat diet) induce ASCs mobilization from AT, leading to their relocation to non-adipose sites. This results in ectopic adipocyte formation and contributes to the development of type 2 diabetes (T2D)[6]. Recently, the frequency of a subpopulation of cells resembling ASCs in the blood of individuals presenting multiple metabolic disorders has been correlated with higher body mass index (BMI), and greater BMI reduction after bariatric surgery, suggesting a similar mobilization process in humans[7]. Despite these findings, the potential predictive value of blood circulating ASCs (c-ASCs), as well as MSCs more broadly, remains poorly understood. So far, standard isolation techniques have struggled to effectively separate c-ASCs from the bloodstream due to several challenges : (i) c-ASCs are rare in blood, with occurrences ranging from few to a hundred cells per millilitre of blood (ii) they exhibit a broad size distribution (10 to 20 µm) (fig S1) (iii) they lack specific unique membrane markers, complicating their identification[8,9] and (iv) studies, including our unpublished findings, suggest that ASCs may circulate in clusters with platelets or leukocytes[10]. Additionally, detecting rare cells using state-of-the-art flow cytometry is challenging due to

[1]LAAS-CNRS, Université de Toulouse, 31031 Toulouse, France. [2]RESTORE Research Center, Université de Toulouse, CNRS, Inserm, EFS, Toulouse, France. [3]Toulouse Biotechnology Institute (TBI), Université de Toulouse, CNRS, INRAE, INSA, Toulouse, France. ✉email: mhbaz@laas.fr; gue@laas.fr

its limited sensitivity in a complex medium such as blood (fig S2). Conventional cell sorting methods often exclude red blood cells (RBCs), leading to the loss of rare cells, and RBC lysis buffers can compromise the integrity of targeted cells. Consequently, establishing a reliable correlation between ASC concentration in the blood and specific physiological or pathophysiological states is exceedingly challenging, resulting in fragile and inconsistent reported data.

Microfluidic technologies may answer this fundamental demand and represent an ideal option for isolating c-ASCs due to their precise control over fluid flow, enabling effective manipulation of rare cells. They are highly sensitive, can handle smaller sample volumes (drops of a sample) with the possibility to handle larger volumes (couple millilitres) through scalable designs. These systems minimize sample loss and are ideal for automated processes with minimal operator handling. One promising approach, negative enrichment, isolates target cells by removing the majority of the undesired cells from a sample. This addresses common issues such as low collection yields due to varying cell surface marker expressions or varying physical and mechanical properties. Negative enrichment can be achieved by label-dependent methods which use antibody-immobilized surfaces[11], channels or beads[12] to deplete unwanted cells or label-free methods that leverage physical properties of cells, such as size or deformability, to achieve sorting. Notably, emerging high throughput methods such as inertial sorting or Dean Flow Fractionation (DFF) rely on channel design to exploit fluid dynamics and achieve high separation efficiency. These methods refined by the works of Dino Di Carlo and Ali Asgar Bhagat[13,14] have enabled isolating different cells from complex mixtures[15,16].

However, to enhance depletion yield, negative enrichment often requires combining complementary methods to isolate cells at rare-event concentrations, 10 to 100 cells. For instance, Bu et al.[17] developed an anti-leukocyte antibody-coated, dual-patterned immunofiltration device to enrich CTCs from RBC-depleted samples. Hyun et al.[18] combined a micromixer with a magnetically activated cell sorter for CTC enrichment. Fachin et al. developed a high-throughput device, which uses deterministic lateral displacement (DLD), inertial focusing, and magnetophoresis to deplete blood cells at a rate of 15–20 million cells per second[19]. Kim et al. recently reported CTC enrichment using a combination of whole blood filtration, immunomagnetic negative selection and dielectrophoretic trapping[20]. Additionally, Zen et al.[21] achieved a two-fold increase in MSC recovery yields from bone marrow aspirates using only a DLD device compared to traditional centrifugation techniques. Thus, the concept of negative enrichment appears well-suited for isolating c-ASCs.

In the present work, we propose a two-step depletion microfluidic approach (ASC-Finder) allowing the isolation and collection of c-ASCs down to 68 ± 35 ASC/mL of blood, paving the way to qualitative and quantitative analysis of c-ASCs in various pathological or inflammatory conditions. This work can lead to advancements in understanding the role of c-ASCs in metabolic impairment and determining whether c-ASCs can be predictive of metabolic impairment or other pathological conditions. Additionally, it can contribute to rare-cell analysis, to the identification of unexpected rare circulating cell subpopulations and consequently to the development of routine diagnosis devices.

Concept of ASC-Finder

The ASC-Finder recovery device consists of two depletion modules (Fig. 1). The first is a size-dependent sorting unit to effectively deplete cells smaller than 10 µm, which are essentially RBCs, platelets and smaller leukocytes. Since RBCs constitute over 99% of blood components, their depletion significantly hinders the efficient isolation of c-ASCs. Hydrodynamic filtration has been chosen as it is well-suited for processing complex media with no sample handling. The second unit involves a Y-Y magnetophoresis module which removes the remaining leukocytes using anti-leukocyte common antigen antibodies (anti-CD45) functionalized magnetic beads.

Hydrodynamic filtration (HDF) module

Ever since its introduction in 2005 by Yamada and Seki, HDF has been widely integrated in microfluidic devices to sort particle mixtures[22]. However, there are few, if any, reports of its use for whole blood processing[23,24]. HDF outperforms similar passive sorting methods such as micro-filtration and deterministic lateral displacement when it comes to filtering dense media as it is less sensitive to clogging/jamming. The reason behind that is

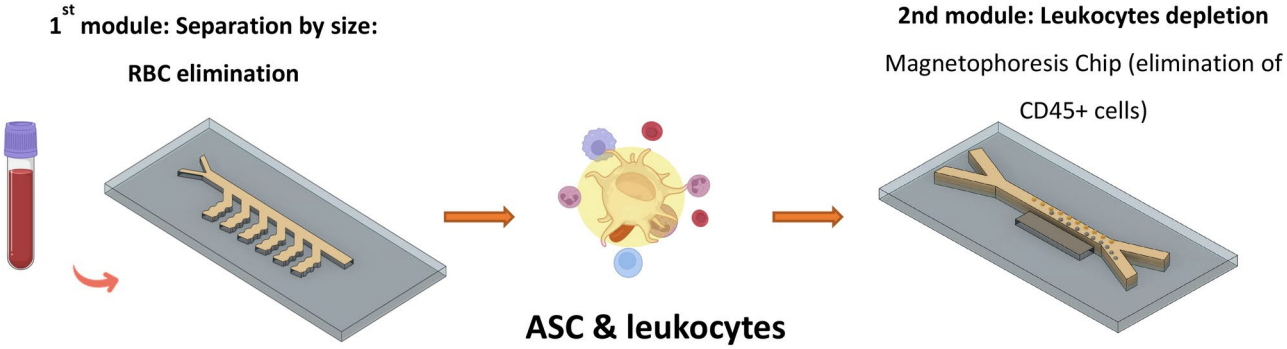

Fig. 1. ASC-Finder device for ASC isolation from whole blood samples portraying the two modules: **1**) the size-based filtration module and **2**) the marker-based separation module. Created using Biorender (biorender.com) and Autodesk fusion360 software (autodesk.com).

the filtration channel dimensions, which can be 2 to 10 times larger than the particle size. This method helps minimize shear stress on the cells and allows the introduction of highly concentrated biological fluids, such as whole blood, into the microfluidic device. Fouling has been shown to occur at high shear forces, primarily due to transmembrane pressure build-up near the membrane[25], which eventually affects particles in the flow[26]. This phenomenon is observed in both traditional and cross-flow filtration methods. Cells in DLD devices are subject to axial shear and frictional forces when they navigate through pillar networks. HDF on the other hand, operates uniquely by the bifurcation law, by strategically splitting the flow at channel bifurcations, particles can be directed into different outlets based on their positions within the flow profile.

HDF can be achieved at any range of pressure drop or flow rate. In contrast to other passive sorting techniques, like inertia-based methods, which require high flow rates and bulkier designs, ultimately lacking sensitivity and facing the same challenges as standard/classical techniques.

The working principle of HDF is depicted in Fig. 2a. In simple terms, if we consider a fluid flowing in a channel network consisting of a main and a single side channel, the portion of fluid flowing through the side channel defines a virtual separating line in the main channel. The distance from this line to the wall of the channel determines the cut-off capacity R_c of the chip. This size-exclusion phenomenon occurs due to the fact that any particle whose centre is positioned between the virtual line and the sidewall of the main channel will exit through the lateral channels and hence be filtered. Particles that are larger than the critical size $R > R_c$ will stay in the main channel and exit using the main outlet.

We can describe the operating mode of the microfluidic chip using electrical analogy (Fig. 2b). As demonstrated by Fouet et al.[27] the separation line is governed by the fraction of fluid Q* flowing in the side channels. Q* is given by the ratio of flow rates of a side channel to that of the preceding segment of the main channel:

$$Q^* = \frac{Q_1}{Q_{in}} = \cdots = \frac{Q_i}{Q_{i-1,i}} = \cdots = \frac{Q_N}{Q_{N-1,N}} \tag{1}$$

where Q_1, Q_i and Q_N are the flow rates of the first, ith and final side channels respectively and Q_{in},$Q_{i-1,i}$ and $Q_{N-1,N}$ represent the flow rates of the main channel segments preceding these side channels as shown in Fig. 2b. Internodal segments of the main channel are kept of constant length all along the chip. Interestingly, it has been shown that the fraction of filtered fluid Q^* is independent of the flow rates or pressure drop in the chip[22]. Hence, given a geometry of the main channel, we can fine-tune the cut-off radius Rc of our microfluidic chip by adjusting the geometry of the side channels.

In the parabolic approximation, Q^* can also be expressed as:

$$Q^* = \left(\frac{R_c}{w}\right)^2 \left(3 - \left(\frac{2R_c}{w}\right)\right) \tag{2}$$

where w is the width of the channel. Considering that the relationship between pressure drop ΔP and flow rate Q is linear, we can introduce the hydraulic resistance of each channel or portion of the channel, $R = \Delta P/Q$.

By analogy with Ohm's law, the pressure-drop between the inlet and the outlet can be expressed as:

$$P_0 - P_{out} = (P_0 - P_1) + (P_1 - P_2) + \cdots + (P_{100} - P_{out})$$

$$R_{in}.Q_{in} + \sum R.Q_{i-1,i} + \cdots + R_{out}.Q_{out} \tag{3}$$

According to Kirchhoff's nodes law, we can express the values of flow rates in each of the internodal segments of the main channel as a function of the initial flow rate Q_{in} and Q^*, as follows:

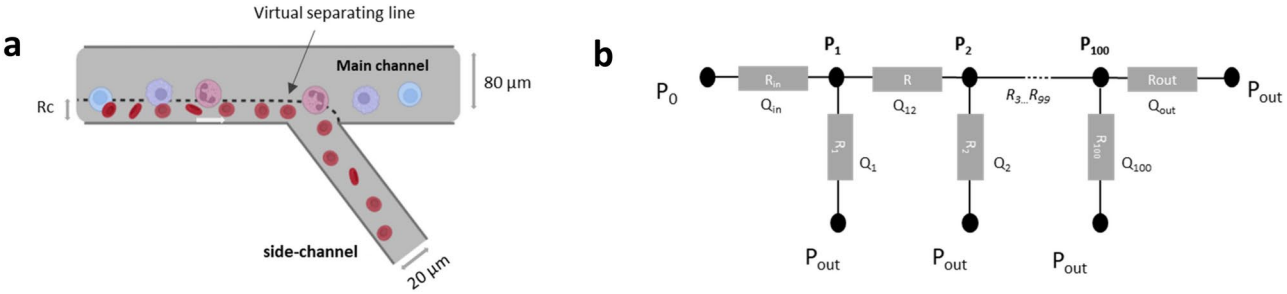

Fig. 2. Presentation of hydrodynamic filtration microchip. **a**) Schematic representation of the size-based filtration of the RBCs in the slanted side-channels with the separating line at the junction representing the cut-off radius R_c **b**) Electrical analogy used to calculate the side channel lengths of the microfluidic chip, where the side channels are represented as resistors (R_1 R_2 R_{100}) each having a value of flowrate Q_1 Q_2 Q_{100} and the main channel is segmented in equal portions having the same value of resistance R (equidistant = equal dimensions) and variable flow rates Q_{12} Q_{23} ..Q_{out}).

$$Q_{i-1,i} = Q_{in}(1 - Q^*)^{i-1} \tag{4}$$

From Eqs. (3) and (4), we can obtain the expression of Q_{in} as a function of the pressure difference across the circuit, the three resistances R_{in} , R and R_{out} as well as Q^*, all of which are constants:

$$Q_{in} = \frac{(P_0 - P_{out})}{\left[R_{in} + R\sum(1 - Q^*)^{i-1} + R_{out}(1 - Q^*)^i\right]} \tag{5}$$

Considering that the flow profile inside the channel is quasi-parabolic, the hydraulic resistance of such channels, R_H can be written as:

$$R_H = \frac{12\mu l}{h^3 w} \div \left\lfloor 1 - \frac{192}{\pi^5}\frac{h}{w} \right\rfloor \tag{6}$$

where μ is the dynamic viscosity of the fluid and , w and h are the length, width and height of the microchannel. If we fix the dimensions of the initial segment, internodal segment distance between the side channels and the outlet segment of the main channel, we can compute their hydraulic resistances using Eq. (6).

From here on, it is possible to compute the flow rates in each internodal segments $(Q_{i-1,i})$ using the general Eq. (4) since they only depend on Q_{in} and Q^* in addition to the pressure drops at each segment of the main channel using generalized formula (7).

for i > 1

$$\Delta P_i = P_i - P_{i-1} \tag{7}$$

After computing the flow rates through each main channel segment $Q_{i-1,\,i}$, we are able to calculate the side channel flow rates Q_i using Eq. (1) and Q^* which was determined earlier. Finally, the hydraulic resistances of each side channel are deduced using Ohm's law (R = Q/ΔP), and consequently side channels dimensions are calculated using the Eq. (6).

Using the calculated dimensions suitable for a 10 µm cut-off chip, the design of the HDF module featured two inlets for the blood and sheath/buffer solutions, two outlets one for the filtrate and the other for the retentate suspensions as well as an array of 100 side channels multiplexed in parallel that will filter out high concentrations of RBCs from complex samples (Fig. 3a). The sheath inlet serves as an additional boundary that hydrodynamically confines the sample flow near the channel's side wall and has a role of flow focusing as shown in Fig. 1. The dimensions of the main channel were fixed at 0.08 × 13.8 mm (w x l) and the section of side channels is 20 × 40 µm as shown in the SEM micrograph in Fig. 3b portraying the serpentine design of the side channels. The corresponding length of the serpentine side channels ranges from 4 to 100 mm. These dimensions are compatible with standard microfabrication technologies and a reasonable footprint of the device (2.5 × 4.5 cm^2).

Magnetophoresis module

The second module consists of a magnetophoresis unit for the selective separation of magnetic particles under the influence of the magnetic field. Magnetophoresis coupling to microfluidics has been extensively described

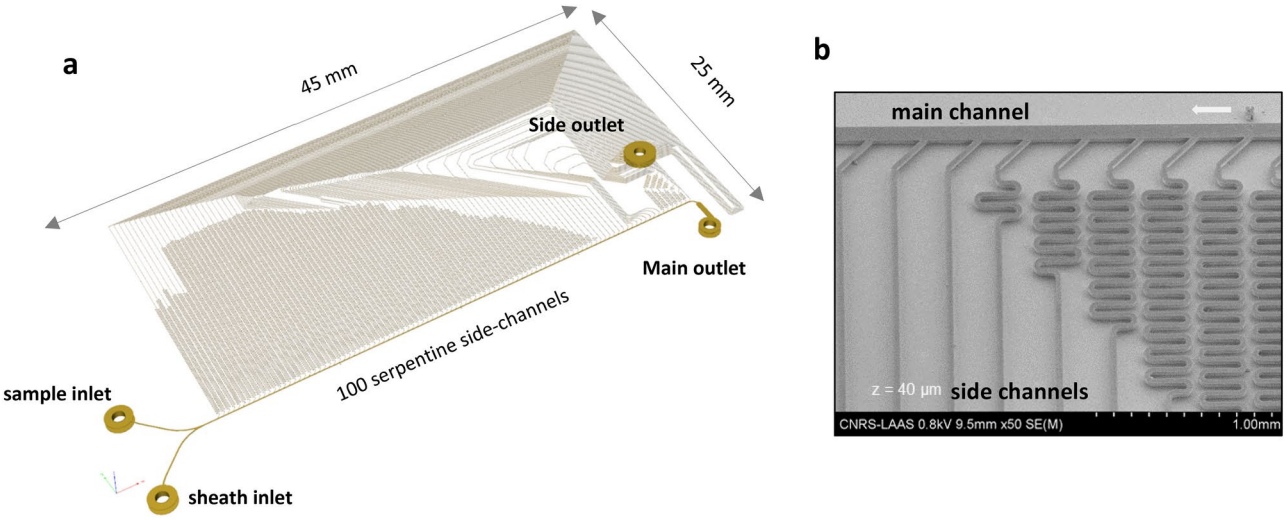

Fig. 3. Hydrodynamic filtration chip **a**) 2.5-D representation of the HF chip, with 2 inlets, 100 side channels and 2 outlets **b**) Micrograph of the last 10 side channels of the chip showing the serpentine structures. Flow direction is indicated by the white arrow.

in the literature. Under the assumption that gravity force is negligible, the resulting forces in the system can be described as follows:

$$\overrightarrow{F} = \overrightarrow{F}_m + \overrightarrow{F}_f$$

where F is the total force exerted on particles in circulation and equals the sum of the magnetophoretic force and the Stokes drag force. $\overrightarrow{F}_m$ can be expressed as:

$$\overrightarrow{F}_m = \frac{V_p \Delta\chi}{\mu_0}(\nabla\overrightarrow{B})B$$

where V_p is the volume of the bead, $\Delta\chi = \chi_p - \chi_f$ are the susceptibilities of the particle and the surrounding fluid, μ_0 is the magnetic permeability of vacuum and $\nabla\overrightarrow{B}$ is the field gradient of the magnetic flux density B. However, in the case of a cell surrounded by magnetic beads, we should take into account the quantity of these particles and their corresponding volumes. This can be iterated as

$$\overrightarrow{F}_{m,cell} = \frac{N_p V_p \Delta\chi}{2\mu_0}\nabla B^2$$

where N_p is the number of particles bound to a cell.

Finally, the force exerted by the fluid $\overrightarrow{F}_f$ in the simplified form, can be expressed as:

$$\overrightarrow{F}_f = 6\pi\eta r u$$

where η and u are the viscosity and velocity of the fluid respectively, considering that the moment of acceleration of the particles is negligible and r is the particle radius.

Based on these relations, we considered that the magnetic force should be of the same order of magnitude as the drag force in order to achieve efficient deviation of the cells. Therefore, the designed module that consists of a Y-Y chip featured a simple channel 20 mm × 200 µm × 100 µm (l x w x h) accompanied by a permanent magnet (Fig. 4). The magnetic field was generated by a permanent neodymium-iron-boron NdFeB magnet (grade N50) that measures 10 × 5 × 2 mm and was positioned in parallel to fluid flow at a distance of 1 – 1.5 mm away from the main channel (Fig. 4a). The remnant field strength $B_r = 1.4$ T. The magnetic field strength over the channel area was tuneable by changing the perpendicular distance between the magnet and the microfluidic chip. The generated field was adequate for efficiently deflecting the tagged cells, with a minimum estimated field strength of 142 mT at the selected distance (1.5 mm), Fig. 4b.

Results

A. Filtration calibration and optimization

The HDF microfluidic chip's parameters have been characterized first experimentally using synthetic samples obtained by mixing two sizes of fluorescent beads (φ = 5 and 15 µm) in phosphate saline buffer (PBS). The inlet pressures P_{sample} and P_{sheath} were chosen so that the sample is completely filtered out through all 100 of the side channels, i.e., to obtain a flow rate permitting total filtration $Q_{sample} = Q_{filtered}$ and were used for the experiments. The sample was introduced in the inlet, along with a buffer at the sheath inlet, in order to establish a laminar co-flow delimiting the sample stream along the filtering side wall of the channel.

This resulted in effective sorting of the larger beads (fig S3) with a recovery yield of 100% using the calculated pressures (fig S4). In contrast, blood, characterized as a non-Newtonian shear-thinning fluid, exhibits a complex rheology and is nearly 4 times more viscous than PBS/bead mixtures. In their numerical analysis, Yoon et al. employed a Bird-Carreau (BC) fluid model to simulate biological fluids in a two-phase flow hydrodynamic

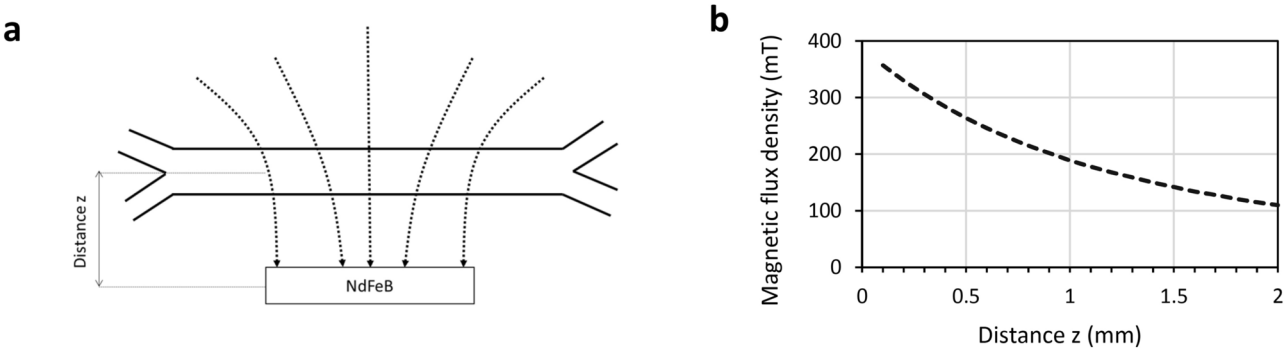

Fig. 4. Magnetophoresis chip **a**) schema of the Y-Y design with the NdFeB magnet at a distance z away from the channel and a representation of the magnetic field lines **b**) magnetic flux density as a function of the distance away from the central channel.

Pressure ratios	$PR_1 = 1.15$	$PR_2 = 1.1$	$PR_3 = 1$
P_{sheath}/P_{sample}	600/520 mbar	550/500 mbar	600/600 mbar
Q_{sample}	1.7 µL/min	5 µL/min	10 µL/min

Table 1. The studied pressure ratios PR at the inlet of the chip with the corresponding sample flow rate values.

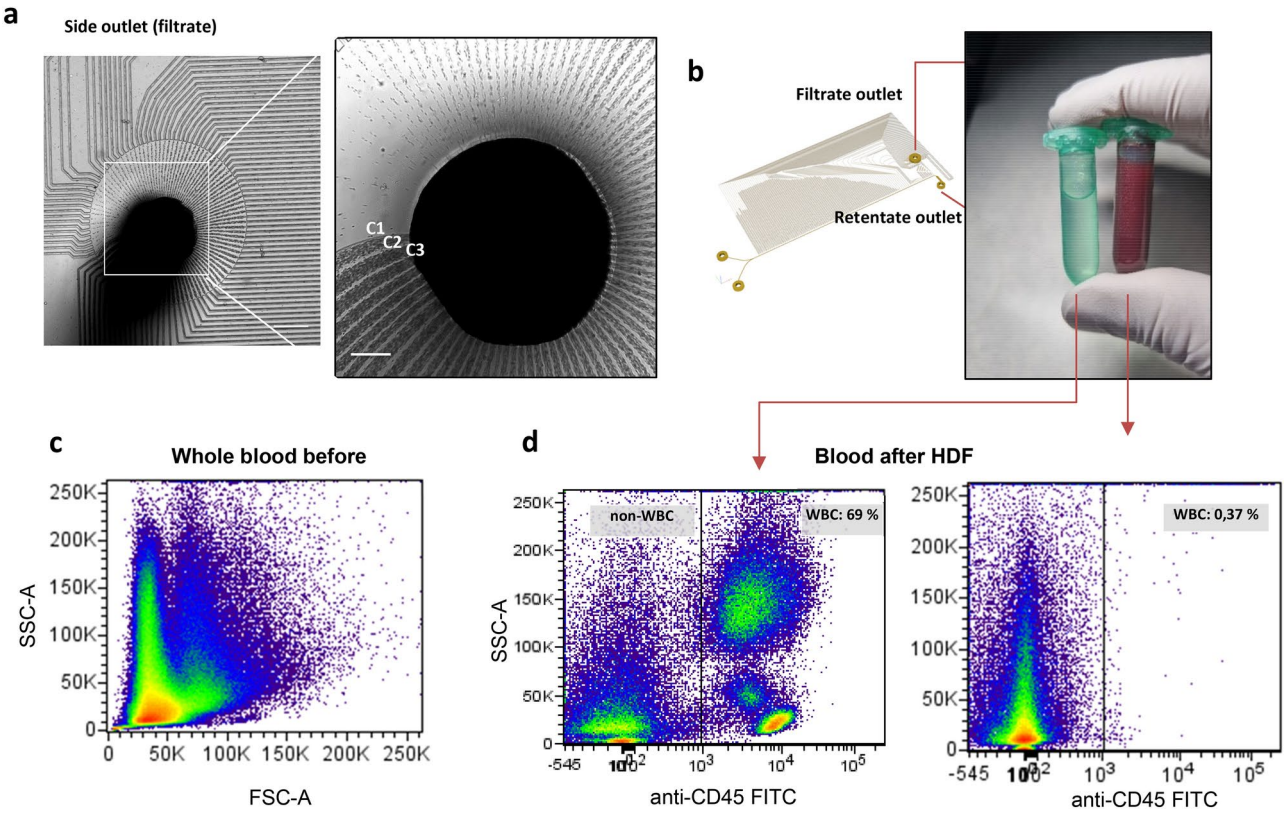

Fig. 5. First module: whole blood filtration experiments **a**) Filtration of RBC at the side outlet. 10 × magnification image at the RBC gradient concentrations from channel 1 to channel 100 Scale bar: 200 µm **b**) the two resulting tubes showing the retentate and the filtrate samples after processing blood in the chip. **c**) Density plots of whole unlysed blood before filtration using the HDF chip **d**) the retentate and filtrate tubes after labelling with anti-leukocyte (anti-CD45) antibody with their respective percentages in each tube.

filtration chip[23]. Interestingly, our experimental results align well with their findings. The fluid–fluid interface at the Y-junction boundary was a key parameter for achieving high filtration yields, necessitating fine-tuning to effectively focus the blood. To validate the HDF module of the ASC-Finder device, whole blood was injected at the sample inlet, while the sheath fluid was introduced at the other inlet under varying pressure ratios, defined as $PR = P_{buffer}/P_{sample}$. The tested pressure ratios were $PR_1 = 1.15$, $PR_2 = 1.1$ and $PR_3 = 1$. The best filtration outcome in terms of RBC depletion was achieved using PR_2. A higher sample flow rate was obtained with PR_3, but considerable amounts of residual RBC remained unfiltered. Good filtration was also obtained using PR_1, but the sample flow rate diminished significantly (fig S4). Therefore, PR_2 was selected as the optimal pressure ratio for the filtration experiments. These results are summarized in Table 1.

A.1 Red blood cell removal efficiency

A crucial index of blood sample reconcentration is the efficient yet gentle removal of RBCs from whole blood. Using the optimized pressure ratio $PR_1 = 1.1$, untreated whole blood was introduced into the HDF module at three flow rates and the resulting outlet tubes were analysed using flow cytometry. Depletion of RBCs from blood was observed by light microscopy in real-time at the level of the side channels shown in Fig. 5a where the side-outlet hole is seen with blood cells pouring out of the 100 side channels. At 10X magnification, a noticeable decrease in RBCs concentration is observed as the fluid progresses through the chip from channels C1 to C100. This visualization reflects the proper functioning of the chip as decreasing gradient of RBCs is expected and logically reflects the removal of blood cells as they move towards the main outlet.

After the complete filtration of an initial blood sample of 0.2 mL, two tubes were obtained, as shown in Fig. 5b—one containing the retentate and the other the filtrate, as indicated by the arrows in the chip schema. The

filtrate tube, collected from the side outlet, had a volume of 1.6 mL and primarily consisted of RBCs and platelets, giving it a distinct red colour. The second tube, containing the retentate, was collected from the main outlet, had a volume of 0.8 mL, and included leukocytes and larger cells, making it appear transparent. Cell composition of both tubes was analysed by flow cytometry in order to calculate the filtration yields. The obtained spectra were compared to a control sample of 2x -diluted non lysed blood (Fig. 5c). Cells were tagged with anti-CD45 FITC and anti-CD235a antibodies specific to leukocytes and RBCs respectively. The cytometry graphs in Fig. 5d show that the majority of the retentate cells are leukocytes representing (59 ± 9%) of the retentate cells in addition to other cells (17% RBCs and 14% non-labelled cells). Complete count of the RBCs was performed to calculate the concentration in the retentate tube. The size-based sorting device achieved RBC depletion rates reaching 99.98% corresponding to (3.6-log reduction) at the optimized flow rates. This was obtained by comparing the RBC concentration in the retentate with that of blood of a healthy individual ($C_{RBC} = 4.5$ to 6×10^9 cell/mL). This highlights the robustness of ASC-Finder device in size-based depletion of unwanted cells.

A.2 Filtration of blood spiked with ASC-mimicking beads

To first confirm the chip's ability to recover 15-µm cells directly from blood, whole donor blood spiked with 15-µm fluorescent beads was used to mimic c-ASCs at two concentration ranges: high (5,000 beads/mL) and low (45 ± 25 beads/mL). The samples were introduced into the HDF module, and the obtained results are shown in Fig. 6. The 15 µm fluorescent beads were observed using live fluorescence microscopy (in real-time) entering the main channel along with blood and exiting exclusively through the main outlet (retentate) *i.e.,* without being filtered (fig S6 & S7) in the serpentines. The beads maintained this path throughout all the experiments proving the efficiency of size selection. Both tubes (filtrate and retentate) were analysed using flow cytometry and fluorescence microscopy without any supplementary fluorescent tags. For high concentrations of beads (5,000 beads/mL), no FITC-positive (FITC+) particles were detected in the filtrate outlet, indicating the complete absence of fluorescent beads (Fig. 6a.). In contrast, the retentate plot clearly shows a substantial number of FITC+events, representing the green fluorescent beads.

For low concentrations of beads (C = 50 ± 25 beads/mL), flow cytometry was excluded due to resolution and technical limitations. Instead, we employed fluorescence microscopy for absolute bead counts in the retentate, as the beads are easily visible in blood samples. Post-filtration, small volumes (V = 200 µL) were pipetted from each tube onto a glass slide and 488 nm wavelength laser excitation was used to detect the beads in each outlet. This method effectively identifies even extremely low bead counts due to the beads' large size and bright fluorescence.

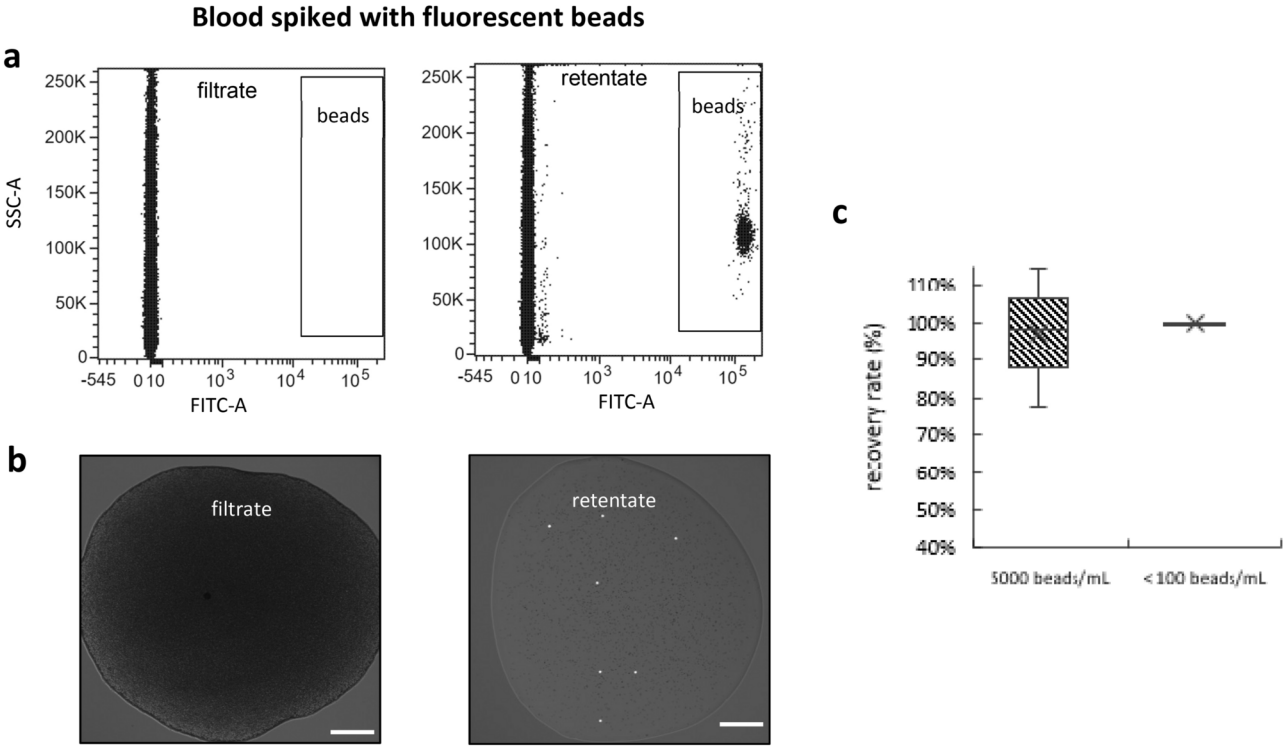

Fig. 6. Whole blood spiked with fluorescent beads side vs main outlets. **a**) µbeads spiked at a 5000 beads/mL. left, SSC vs FITC scatter plot showing no FITC+beads. Right, scatter plot of the retentate tube showing the presence of FITC+events indicating the green fluorescent beads. **b**) µbeads spiked at < 100 beads/mL, analysis done using fluorescent microscopy images (488 nm laser excitation) of a 200 µL drop of each tube obtained after filtration in the chip. Left, filtrate drop, absence of any fluorescent bead. Right, retentate drop, large bright beads among the filtered cells, scale bar: 200 µm c) recovery rate of beads from whole blood at 5000 bead/mL and at 100 beads/mL portraying 100% recovery rate.

Figure 6b shows the composition of the outlets with no fluorescent beads observed in the filtrate indicating the absence of fluorescent beads. In contrast, the retentate drop contains the fluorescent beads which proves that our device is capable of recovering beads at low counts.

The recovery rates of beads spiked in blood reached 97 ± 18% at higher concentration (5000 bead/mL). Although we anticipated 100% recovery during live microscopy in the experiment, we suspect that the slight variation may be due to pipetting errors in the initial concentration or variations in cytometry readings. For rare-event concentrations on the other hand, we obtained 100% recovery yields after total enumeration of the tubes using fluorescence microscopy (Fig. 6c). This was reproducible in samples spiked with rare-event concentrations of fluorescent beads (50 ± 25 beads/mL $N = 3$) and confirms that our HDF module effectively recovers rare events in whole blood while respecting the preselected cut-off diameter.

B. ASC isolation experiments

After validating the module's capacity to recover larger particles (15-µm beads) directly from blood, experiments with primary fluorescent ASCs were done at high (10^4 – 5×10^4 ASC/mL) and low concentrations (68 ± 35 ASCs/mL). The samples were first filtered using the HDF module and both outlet tubes were analysed by flow cytometry and microscopy as described in A.2. The experimental workflow is summarized in Fig. 7a. Additionally, a portion of the retentate was kept for further cell culture and adipogenic differentiation assays.

B.1 Blood spiked GFP-fluorescent ASCs

Fluorescent ASCs were spiked directly into blood samples at high (10^4 – 5×10^4 ASC/mL) and rare-event concentrations (68 ± 35 ASC/mL) then filtered in our device to assess recovery rates. Flow cytometry allowed for the direct identification of fluorescent ASCs in the retentate tube as GFP + particles, enabling precise assessment of their recovery. The scatter plots comparing the filtrate and retentate tubes are shown in Fig. 7b and demonstrate that ASCs from the native sample are exclusively present in the retentate tube, comprising 16% of the total cell count in that tube. This represents a 1:6 ratio of ASCs to blood cells at this outlet, and a 2666-fold enrichment of ASCs at this concentration. In contrast, no ASCs are detected in the filtrate tube, indicating that few to no ASCs are recovered in the main outlet.

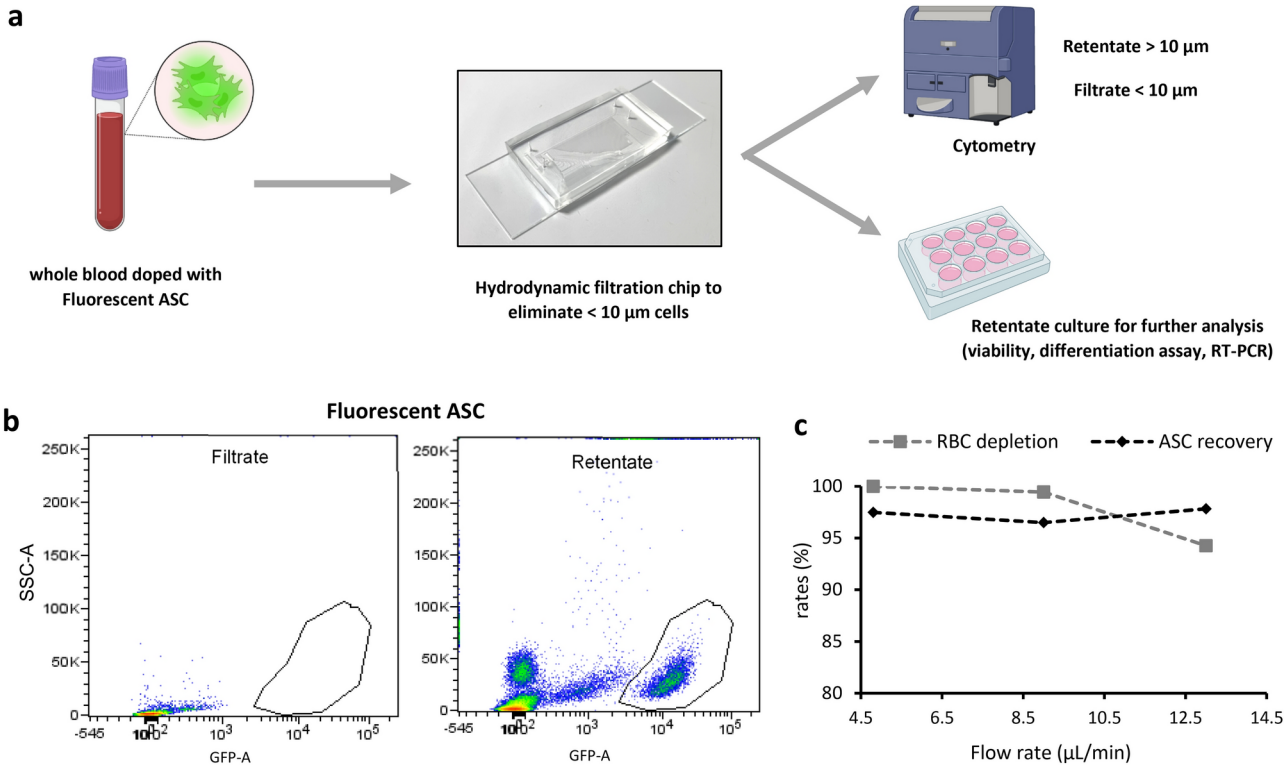

Fig. 7. Filtration experiments of ASC – doped blood **a**) Schematic depicting the work-flow of the filtration and analysis experiments of fluorescent ASC from whole blood samples. **b**) ASC filtration from whole blood samples. Left, SSC vs FITC density plots of the filtrate tube (side-outlet), depicting absence of any GFP + event in the preselected gate, indicating absence of fluorescent ASC. Right, SSC vs FITC density plots of the retentate tube, with the GFP + fluorescent ASCs highlighted in the gate. **c**) RBC depletion and ASC recovery rates as a function of inlet flow rate. ASC recovery is not impacted by the flow rate in the HDF chip with > 96% ASC recovered. Retentate purity is impacted on the other hand, with a decline in RBC depletion rate reaching 95% at 13 µL/min.

For rare-event concentrations (68 ± 35ASC/mL of blood), flow cytometry was not used to quantify recovery and depletion rates. Instead, fluorescent microscopy was employed and recovery rates and depletion rates in the retentate were quantified using the following formulas:

$$R = \frac{N_{outlet}}{N_{inlet}} \times 100\% D = 100\% - R$$

where N is the number of cells/particles of interest. Similarly, if we subtract the recovery rate from 100%, we obtain the depletion rate D.

The samples originating from the retentate tubes were left to sediment for 5 min in 48-well cell culture plates before complete enumeration of the whole volume. RBC depletion and ASC recovery rates as a function of inlet flow rate are shown in Fig. 7c. We observed that ASC recovery is not impacted by the flow rate in the HDF chip with > 96% ASC recovered at all the tested inlet flow rates. Retentate purity is impacted on the other hand, with a decline in RBC depletion rate reaching 95% at the highest tested flow rate (Q = 13 µL/min).

These experiments demonstrate the HDF module's capability to directly enrich blood-borne circulating ASCs at both high and low concentrations (below 100 ASC/mL) without requiring blood pre-treatment, such as lysis or centrifugation cycles which could compromise the integrity/functionality of these rare cells.

B.2 Post-filtration: ASC culture—expansion ability

To ensure the viability and functionality of the filtered ASCs, subsequent analyses were conducted to verify that the cells maintained their integrity post-filtration (Fig. 8). The results were compared to control samples of the same ASCs that had not undergone filtration through the HDF module with both sets of cells isolated simultaneously.

At day 1 (D1), adherent cells started adopting an expected fibroblastic shape morphology, with the majority adopting the round shape (Fig. 8a). Both control and retentate-derived cells achieved 70 ± 5% confluency after 1 week of culture (Fig. 8b). At confluence, the cells of both groups adopted the expected spindle-fibre morphology typically seen in MSCs.

These culture experiments prove that even though the spiked primary cells can be fragile when exposed to mechanical stresses (compared to cell lines), they showed excellent adhesion and replication after filtration in the HDF module. This shows that our device has no impact on ASC function (self-renewal) which was compared with control groups.

B.3 Post-filtration: ASC differentiation

Upon reaching 80% confluency, the plating culture media for both the retentate and ASCs (standard DMEM supplemented with FBS 10% and PS 1%) were replaced with adipogenic medium to assess differentiation (Fig. 9). At day 1 of media change, the cells in the differentiated well started accumulating lipid droplets indicating their differentiation into adipocytes, conversely to the cells in the control wells (Fig. 9a). A gene expression analysis focused on three key adipogenic genes—adipocyte protein 2 (aP2), lipoprotein lipase (LPL), and Peroxisome proliferator-activated receptor gamma 2 (PPARɣ2)—was conducted four days post the initiation of adipogenesis.

Cells in the differentiated wells showed 90, 24 and 20-fold increase for AP2, LPL and PPARɣ2 genes respectively compared to their control ND (non-differentiated) counterparts which indicates that the cells of the retentate are indeed ASCs with full differentiation potential conserved and functional (Fig. 9b).

These experiments prove that the HDF module has little to no impact on ASC integrity. Nonetheless, they were only performed using high-concentrations of initial ASCs spiked in blood, yielding sufficient cells for plating, proliferation, and differentiation assays. After validating the HDF chip's efficacy, rare-cell concentrations

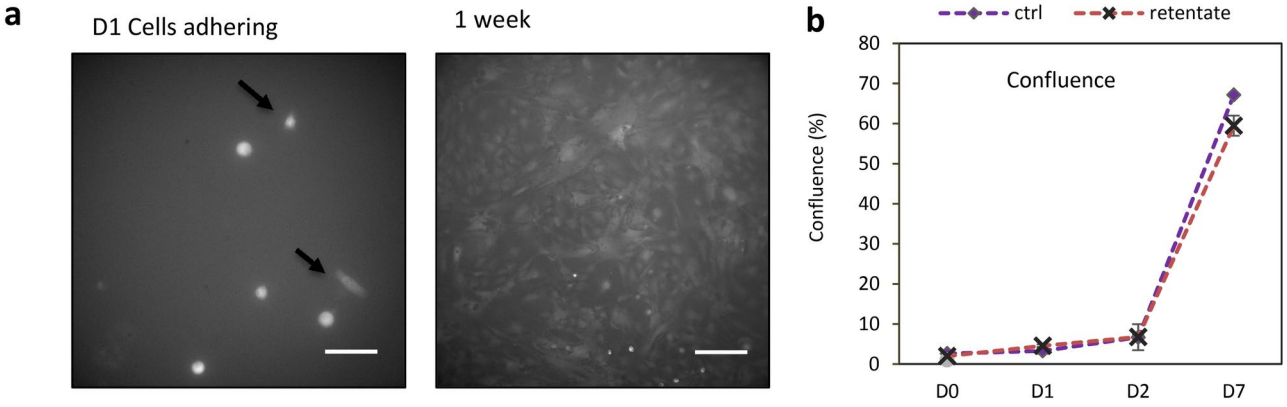

Fig. 8. Retentate cell culture and viability assay. **a**) retentate cells plated in culture wells at D0. Fluorescence microscopy images at D1 showing ASCs adhered to culture well, black arrows showing fibroblast like cells. After 1 week, GFP fluorescent cells at confluence in the retentate well adopting fibroblast morphology, scalebar 100 µm **b**) confluence line graphs showing the increase cell/surface ratio of both cell groups in the culture wells as a function of time during cell culture.

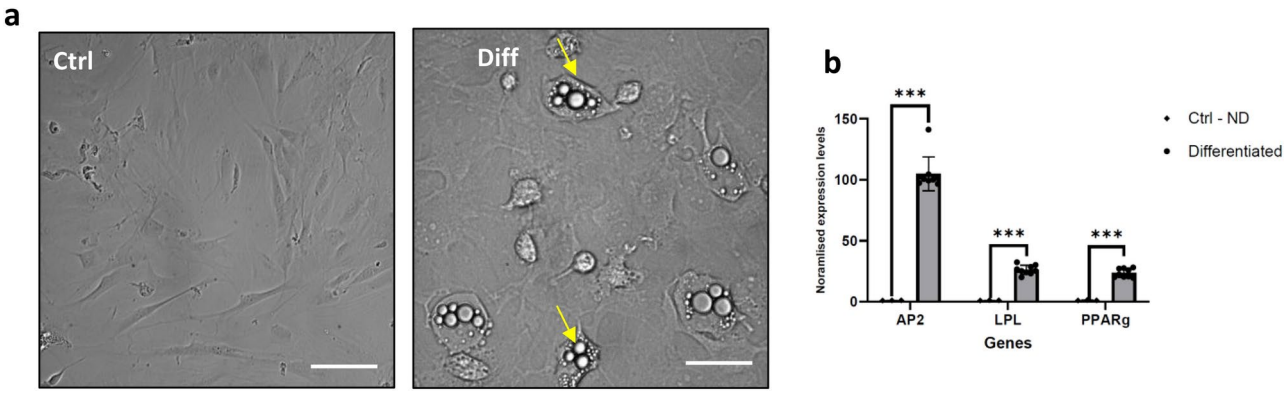

Fig. 9. **a**) ASC differentiation assay. left, image of ctrl cells showing the spindle-shape typical of adipose stromal cells in vitro right, image of differentiated cells showing the accumulation of lipid droplets highlighted by yellow arrows, scalebar 100 µm **b**) normalised gene expression of AP2, LPL and PPARg2 in control-non differentiated cells (ND) and differentiated cells.

(< 100 ASC/mL) were tested using the magnetophoresis chip. However, post-filtration cell yields were insufficient for viability and differentiation assays due to low seeding densities. Thus, these assays were performed prior to magnetophoresis, where ASC concentrations were adjusted to ensure adequate cell numbers for analysis.

C. Immuno-magnetic depletion of leukocytes on chip

After size-based sorting of whole blood spiked with low counts of fluorescent ASCs, the retentate tube was then injected in the magnetophoresis chip for depletion of CD45 + cells. CD45, also known as the leukocyte common antigen, is a transmembrane protein expressed on the surface of all nucleated hematopoietic cells, including all types of leukocytes (white blood cells), but is absent on mature erythrocytes (red blood cells). Given that CD45 is expressed on all leukocytes, targeting and removing CD45-positive cells from blood effectively eliminates the entire leukocyte population (lymphocytes, granulocytes and monocytes). The retentate cells were incubated for 30 min with a suspension of anti-CD45 coated magnetic beads (Ø = 4.3 µm) to deplete remaining WBCs. The concentration of beads was used according to the fabricant's instructions *i.e.,* each cell having a minimum of 5 beads bound to it. After incubation, the resulting tube was then introduced at two flow rates, Q1 = 60 µL/min and Q2 = 30 µL/min in the magnetophoresis module for efficient deviation of the bead-bound leukocytes.

The permanent NdFeB magnet (grade N50) was initially positioned parallel to fluid flow at a distance of 1 – 1.5 mm away from the main channel (Fig. 10a-i). In these configurations and distance, we were able to maintain homogeneous and continuous circulation of the sample in the chip. The cells decorated with the anti-CD45 beads were continuously deviated and visible near the wall of the channel attracted by the magnet nearby (Fig. 10a-ii). Leukocyte counts in both tubes were obtained, and leukocyte depletion rates were calculated by comparing final to initial counts in blood using fluorescence microscopy.

Both the ASC and the leukocyte tubes were analysed to determine the remaining number of residual leukocytes in the ASC tube and to enumerate the number of isolated ASCs. After magnetophoresis, both tubes were pipetted in cell culture wells (12 well-plates $S_{well} = 1.1\ cm^2$) and were analysed using fluorescence microscopy. Figure 10b shows the bead-bound cells (CD45 + leukocytes) that are driven towards the magnet, as expected 92.5% of the cells decorated with the anti-CD45 beads resulted in the leukocyte side, whereas the free cells which are only confined hydrodynamically (using the sheath/buffer) resulted in the ASC outlet. We noticed however a tiny fraction of beads or bead-bound cells escaping through the ASC outlet (< 2.5%). The spiked fluorescent ASCs are easily visible in the wells in addition to some other cells (CD45- cells). We suspect them to either be residual RBC/WBCs or other rare cells in circulation.

After the whole two-step process, we obtained 82.28 ± 2% depletion rate of leukocytes in the final ASC tube sign Q1 rate and 92.55 ± 1.8% depletion of leukocytes using the optimized flow rate Q2 Figure 10c. The final ASC recovery rate after the two-step process reached 81% for extremely low counts of ASC in blood (68 ± 35 ASC/mL).

Figure 10d recapitulates the evolution of ASC counts during the whole process. It shows the initial number of spiked fluorescent ASCs in whole blood tubes (named before). Three trials of rare ASCs were performed with initial numbers 92, 85 and 28 ASCs spiked originally into 1 mL of whole blood for the. This number was quantified after each of the two subsequent depletion steps (HDF module) and magnetophoresis. After the HDF step, we were able to recover 96 ± 3% of the originally spiked ASCs at very low numbers. After the two-step depletion, and for all three trials, the ASC recovery rates exceeded 81 ± 4% of the originally spiked quantity. This highlights the capacity of the device in preserving rare-events of circulating ASCs after two steps of negative sorting enabling their direct detection and isolation from whole untreated blood.

Following the depletion of RBCs and WBCs from whole blood samples, the enrichment factor of the recovered ASCs was quantified. Initially, the ASC-to-blood cell ratio in the blood samples was determined to be $1:2 \times 10^8$, where blood cells represent the combined refer population of WBCs and RBCs in a healthy donor's blood. After the implementation of the two-step depletion process, the final ratio was reduced to $1:1 \times 10^5$ blood cells,

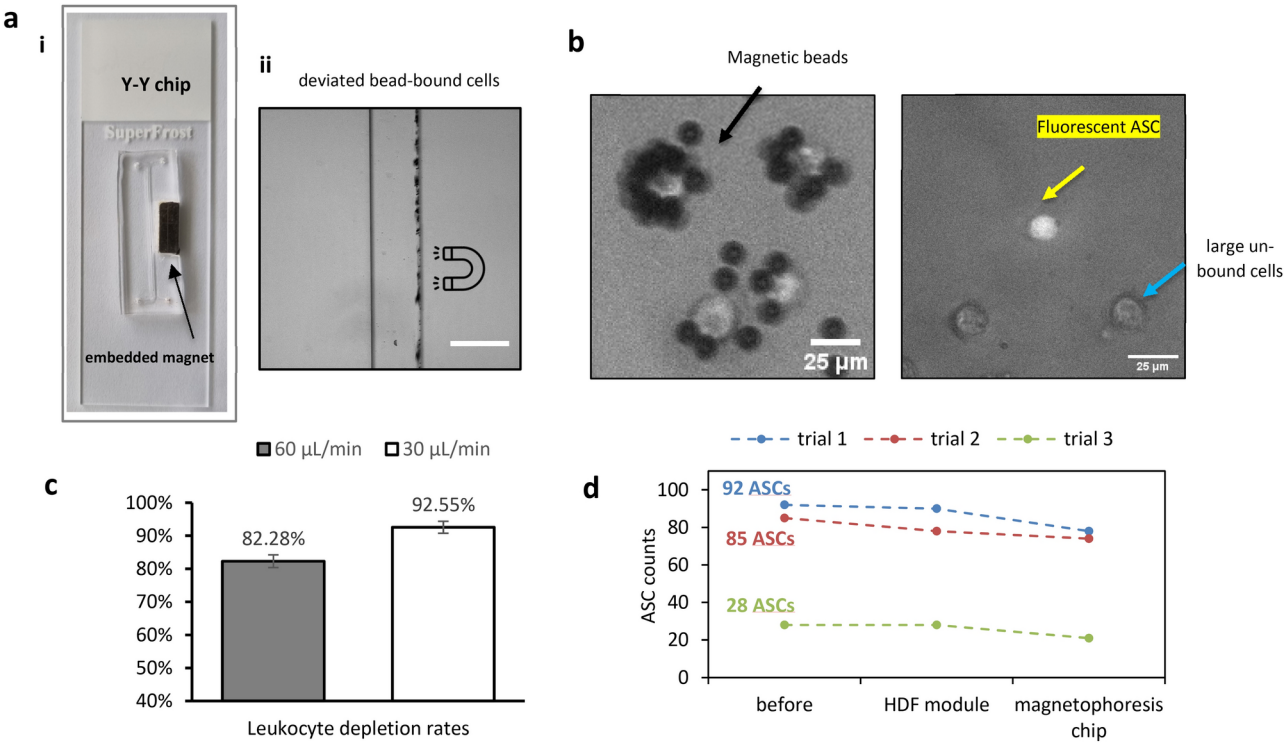

Fig. 10. Magnetophoresis module and experiments. **a**) i—PDMS chip mounted on the microscopy slide with the integrated permanent magnet. ii—chip main channel demonstrating the magnetic beads in flow deviated by the nearby permanent magnet. **b**) microscopy images showing the bead bound cells (CD45 + cells) in the leukocyte outlet and the fluorescent ASCs in the ASC side after treatment in the magnetophoresis chip. **c**) leukocyte depletion rates using the two tested flow rates in the microfluidic chip. **d**) total ASC recovery in absolute counts, in the beginning of the process, after stage 1 HDF module; and after stage 2 (magnetophoresis module).

corresponding to an average enrichment factor of 1,750-fold for ASCs. This significant enrichment underscores the efficacy of the depletion strategy in isolating rare ASC populations from complex blood samples.

Discussion

The ability to isolate c-ASCs from blood represents a real challenge, given their potential for tissue repair[28], immune modulation[29], and diagnostics. Moreover, these cells are not only valuable for therapeutic applications but may also serve as biomarkers, including disease monitoring and progression, as we and others have reported in cases of metabolic disorders such as type 2 diabetes[30]. The potential of c-ASCs extends beyond diagnostics and therapy, making their study crucial for developing new therapeutic strategies. Despite their clinical relevance, there is a notable lack of specialized devices for isolating c-ASCs from blood due to their low abundance and the technical challenges associated with separating them from other blood components. Fluorescence Activated Cell Sorting (FACS) for instance, is considered a robust method for cell sorting; however, our flow cytometry analyses revealed significant limitations in its ability to detect rare cell populations within untreated samples like whole blood (Fig. S2). Specifically, detection of fluorescent ASCs in whole blood proved ineffective even at elevated concentrations of 0.5 million ASCs/mL (Fig. S2c). Following red blood cell (RBC) lysis, the sensitivity of detection improved, enabling identification at concentrations as low as 5000 ASCs/mL (Fig. S2e). This underscores the influence of sample matrix complexity on detection thresholds. Nevertheless, reliable detection remained unachievable at concentrations below 5000 cells per mL of lysed blood (Fig. S2f.), highlighting a critical sensitivity constraint under these conditions.

In this study, we present the ASC-Finder, a two-step sorting microfluidic device designed to enrich and isolate c-ASCs from whole blood. Its primary goal is to validate the presence of cASCs, so the performance of ASC-Finder was first evaluated under controlled, healthy conditions. While the long-term objective of the study encompasses the use of diabetic or other disease mouse models, introducing such models at this initial stage would have introduced confounding variables, as the behavior of cASCs in type 2 diabetes (T2D) remains poorly characterized and can vary widely across different mouse models. Validating the device in a standardized, healthy environment was a critical step to establish its reliability before applying it to more complex pathological conditions. This foundational validation was essential to ensure accurate and consistent results before progressing to investigations of cASC dynamics in T2D, including tracking their levels during disease progression and assessing their functional potential.

The ASC-finder device operates through two mechanisms: first, the HDF module, which efficiently removes smaller cell bodies such as RBCs and platelets; and second, an immunomagnetic sorting chip that depletes remaining leukocytes, thereby isolating c-ASCs with high specificity. To our knowledge, no other device has successfully recovered c-ASCs directly from whole, non-lysed blood. While other teams, such as Zhu et al.[31], Abdulla et al.[32], and Nivedita et al.[33]., have reported high depletion rates and separation efficiencies using microfluidic techniques, these methods either excessively dilute blood samples or rely on RBC lysis to achieve separation. One of the ASC-Finder's most significant advantages is that it minimizes sample handling by treating whole blood directly, without requiring RBC lysis or dilution. RBC lysis is known to negatively impact cellular physiology and activate some cell populations, which can introduce artifacts in downstream analyses. Moreover, the process of lysis often results in significant cell loss, as seen in previous studies where leukocyte loss ranged up to 11% when lysis-based protocols were used[32]. In contrast, our direct filtration method not only reduces cell loss but also maintains the integrity of the c-ASCs, which is crucial for their further functional analysis.

The HDF module in the ASC-Finder demonstrates superior filtration efficiency compared to similar devices due to several key design features. First, the innovative design of the HDF chip minimizes clogging by incorporating side channels instead of filtration pores. Unlike traditional filtration systems that rely on porous membranes—prone to saturation and blockage—the HDF chip utilizes a strategic flow diversion mechanism to achieve separation. This design allows the filtration channels to have dimensions larger than the target particle size, reducing clogging risks while maintaining efficient separation. Second, the slanted or oblique orientation of these channels, rather than a perpendicular connection to the main channel, further enhances performance by preventing flow instabilities and minimizing shear-induced effects commonly observed at right-angle bifurcations. This structural arrangement ensures smoother fluid dynamics and sustained filtration efficiency. Third, the use of a buffer containing BSA and EDTA significantly reduces clotting and aggregate formation along the channels and walls compared to Phosphate Buffer Saline (PBS). Notably, this improvement is achieved without requiring any pre-preparation steps or PDMS coating. While platelet-induced coagulation due to shear forces remains a potential challenge, the overall design of the HDF module effectively mitigates other common issues, ensuring stable flow dynamics and enhanced filtration performance.

The achieved depletion, approximately 3.6-log depletion of RBCs, is lower than the 5-log reduction reported in other microfluidic systems, is adequate for the biological objectives of this study. Although previous works have developed devices capable of achieving higher levels of RBC depletion, it is important to note that no microfluidic platform currently exists specifically for the isolation of c-ASCs directly from whole blood. For the purposes of c-ASC analysis (e.g., genomic analysis, immunophenotyping) the presence of some RBCs does not impede the identification or characterization of the target cells. Thus, the current performance of the HDF module is more than sufficient for this stage of development. However, achieving a 5-log RBC reduction remains a target, as high RBC levels can contribute to the total cell load, potentially increasing the sequencing efforts required to detect other cell populations in single-cell or RNA sequencing approaches.

Our experiments revealed that filtration efficiency was optimized at a critical inlet flow rate, deviating from conventional HDF theory, which suggests that filtration is flow rate-independent. This deviation could be explained by the influence of deformability-induced lift forces, which dominate in diluted blood suspensions and therefore may become significant in the downstream part of the main channel where the sample is RBC depleted[34]. By reducing the inter-branch distance within the device, we anticipate further improvements in filtration efficiency and a reduction in device length, enhancing overall performance. Another adjustment would be to implement a dual inlet chip for blood and sheath with a Ψ-shaped entry. This allows for sheath to enter through the middle and to hydrodynamically focus blood onto both sides of the main channel. This enables filtration to occur on the top and bottom using serpentine branch-channels, dividing the processing time by 2. Other teams augmented filtration throughput in their devices by stacking their devices in parallel, which can be easily implemented for our HDF modules. This would augment sample treatment rate by a factor of 5 × and guarantees high viability of cells during the procedure.

The leukocyte depletion module of ASC-Finder leverages 4.5 µm magnetic beads to label non-target cells (leukocytes) for c-ASC sorting. This straightforward approach uses a permanent magnet embedded in a PDMS chip, adjacent to the microfluidic channel. However, devices employing magnetophoresis often encounter issues such as magnetic field inhomogeneity, with field spikes at certain locations along the chip[35]. This uneven distribution can cause inefficient cell sorting or clogging in microfluidic systems. To address this, we optimized the design by incorporating a smaller magnet and extending the length of the microfluidic channel. This solution enhanced the consistency of magnetic field exposure, ensuring continuous flow while maintaining efficient leukocyte depletion. This design contrasts with more complex systems that utilize microfabricated magnets or magnetized structures within the channel, which, although effective, increase system complexity and cost, defeating the purpose of a low-cost, accessible device. ASC recovery rates obtained using our device neighbour 100% after HDF, the major loss of ASCs occurring during the process of magnetophoresis. We suspect that this loss is largely due to manual handling steps, including sample incubation and transfer between chips, rather than inherent deficiencies in the magnetophoresis process itself. This suggests that further refinement is needed, particularly through automation and process integration, to reduce human intervention and variability, which would improve consistency and cell recovery. It is worth noting that, even with these challenges, our device consistently achieved high yields, recovering 81 ± 4% of the original rare ASCs. This performance is significantly higher than what is typically reported with traditional methods, which often suffer from higher cell losses due to suboptimal magnetic separation or more complex device designs[20].

Given the rarity of circulating stem cells, it is critical to minimize "contamination" from abundant blood cells (e.g., red blood cells, leukocytes) to enhance the sensitivity and specificity of our analysis. While achieving 100% depletion of all residual cells is practically impossible, our two-step approach significantly reduces their presence, thereby improving the likelihood of detecting and characterizing these rare stem cell populations. This

strategy is essential to avoid masking or diluting the signal from circulating stem cells especially in the context of downstream analysis. By prioritizing near-complete depletion, we aim to maximize the purity of our sample and ensure the reliability of our findings in studying these rare and biologically significant cells.

Most importantly, our results show that the ASCs retain their ability to proliferate and to differentiate into fat cells, two fundamental aspects of their biological role after the critical HDF filtration step. This suggests that the ASC-Finder maintains the functional integrity of rare c-ASCs, thus providing a powerful platform for large-scale characterization and putative clinical applications. These findings highlight the efficacy of our two-step approach in enriching low concentrations of ASCs, offering a valuable tool for rare-cell analysis. The ability to study c-ASCs holds promise for advancing our understanding of these rare cell populations and their association with various disorders, paving the way for potential breakthroughs in both research and clinical applications.

Materials and methods

A. Lab on chip fabrication

Both microfluidic chips were fabricated using a standard photoresist—PDMS moulding technique.

Hydrodynamic filtration wafer—Resin mold: The microfluidic patterns were obtained by lithography using dry film negative photoresists (commercial DF-10XX series). Using a spin coater, GLYMO silane ((3-Glycidoxypropyl) trimethoxy silane) was applied on a clean plasma treated 4″ silicon wafer as an adhesion promoter. The (40 µm or 100 µm) DF was then laminated using a Shipley 3024 laminator at 100 °C with a pressure of 2,5 bar and at a speed of 0,5 m/s. The wafers were UV exposed with the photomask using the MA6 mask aligner (Suss Microtec). After photolithography, each wafer was baked at 100 °C for 10 s on a hotplate, then developed in two cyclohexanone baths for 7 min then cleaned with isopropanol. An additional surface functionalization step with SiO2/Perfluorodecyltrichlorosilane (FDTS) was required before PDMS moulding to facilitate PDMS demoulding.

PDMS molding and chip bonding PDMS mixture was obtained by mixing the elastomer (Sylgard) and curing agent ratio 1:10. After degassing, the mixture was poured onto the mold and cured during 1 h at 60 °C. Then individual devices were diced and peeled off of the silicon wafer mold. The PDMS was then punched using 0.75 mm punchers to define the inlets and outlets of the chips. The chips were exposed to oxygen-plasma for 40 s at 0.25 mbar in a plasma oven prior to being bonded onto clean glass microscopy 25 × 75 mm slides.

B. Chemical and biological reagents

AutoMACS® running buffer (Miltenyi 130–091-221) was used as running sheath in the chip for the RBC sorting experiments from whole blood.

15 µm (505/515 nm) and 4 µm (580/605 nm) polystyrene fluorescent beads were bought from Invitrogen and were used for the preliminary filtration tests of the HDF module. Formaline (Sigma HT5012) was used to fix the cells before antibody labelling (Miltenyi). anti-CD45-FITC human and anti-CD235a (Glycophorin A)-PE human were used to label the leukocytes and the RBC respectively.

Dynabeads anti-CD45 (11153D—thermofisher) were used for leucocyte labelling. 30 µL of the stock solution was added to the cells and incubated for 30 min at room temperature.

C. Microfluidic experiments

In both modules, fluid flows were controlled by a pressure generator (Fluigent MFCS). The inlet pressure was varied from 0.5 to 1.45 bar for the filtration experiment and from 40 to 65 mbar for the magnetophoresis module. The outlet tubes were left at atmospheric pressure. The chips were first filled with running buffer (autoMACS) sheath to remove air bubbles from the microchannels then the samples were introduced. The chips were placed on an inverted fluorescence microscope for data acquisition during the experiment. Outlet tubes were stored at 4°C after fixation with Formaline for further fluorescence analysis.

D. Blood samples

Blood samples were obtained from l'Etablissement Français du Sang (EFS) in 4 mL tubes containing EDTA. They were stored at 4 °C before manipulation and filtering in the device. After manipulation, the two outlet tubes (filtrate and retentate) were fixed with 4% Formaline and kept at 4 °C until their analysis by flow cytometry the day after.

RBC lysis experiments were done using ammonium chloride solution as the lysis buffer: 0.15 M NH4Cl, 10 mM NaHCO3 and 1.4 mM EDTA. 1 mL of blood was diluted in this solution at 1:15 (blood: lysis buffer) homogenized and left at RT for 10 min. The tube was then centrifuged at 400 g for 10 min at 4 °C. The supernatant was then discarded and fresh PBS was added for cytometry analysis.

E. ASC isolation experiments

All experimental procedures were approved by the Regional Ethics Committee and registered with the French Ministère de la Recherche and all methods were performed in accordance with the relevant guidelines and regulations**.** The study complies with the relevant ARRIVE guidelines for animal research reporting.

The mice used in this study were bred and housed in our laboratory in Restore Lab in Toulouse, France. Male C57Bl/6J mice aged 8–12 weeks were housed under controlled conditions: 12-h light/dark cycles (07:00–19:00), temperature of 20°C–22°C, and hygrometry of 40% ± 20%, with ad libitum access to a chow diet (8.4% fat, Safe® A04, Safe lab). Mice were anesthetized with 4–5% isoflurane in oxygen, and once fully sedated, blood was collected from the inferior vena cava using a G25 needle and 1 mL syringe pre-coated with PBS/heparin (20 U/mL). Following blood collection, cervical dislocation was performed, and subcutaneous adipose tissue (ScAT) was immediately harvested for ASC isolation.

The Harvested subcutaneous AT (ScAT) were likewise obtained from male fluorescent transgenic mice (the KIKGR model). ScAT were minced and digested with collagenase (NB4, Coger; 0,4 U/mL) and DNAse (1%, Roche) in αMEM (GIBCO) at 37°C for 45 min under constant agitation. After centrifugation (300 g, 10 min, room temperature, RT) and elimination of the floating mature adipocytes, the pellet containing the SVF was resuspended in erythrocyte lysis buffer (155 mmol/L NH4Cl; 5,7 mmol/L K2HPO4; 0,1 mmol/L EDTA, pH 7.3) to remove red blood cells. After filtration (34 µm sieve) and centrifugation (300 g, 10 min, RT), SVF were resuspended in PBS/0,5% bovine serum albumin (BSA)/2 mM EDTA. Freshly harvested AT-derived SVF were used for cell sorting.

To sort ASCs, ScAT-derived SVF were depleted in CD45 + and CD31 + cells using anti-CD45-FITC and anti-CD31-FITC antibodies followed by anti-FITC magnetic microbeads using an autoMACS® Pro Separator (MACS Cell Separation, Miltenyi Biotec SAS) according to the manufacturer's instructions. CD45-/CD31- cells were then positively sorted for Sca-1 with anti-Sca-1 magnetic microbeads.

F. ASC adipogenic differentiation assay

ASCs were plated at 2.5×10^4 cell/mL in DMEM supplemented with 10% fetal bovine serum (FBS) and 1% penicillin/streptomycin at 37 °C 5% CO2. At confluency, the medium was replaced by a differentiation medium containing human insulin (5 µg/mL), triiodothyronine (2 ng/mL), apotransferrin (10 µg/mL), dexamethasone (33 nM) and rosiglitazone (2 µM). Medium was changed every 3 days and for a total duration of 20 days until the RT-PCR assay.

G. Isolation and real-time RT-PCR analysis

Total RNA was extracted using the Quick-RNA MicroPrep Kit 200 preps ZR1051 (Zymo) following manufacturer's instructions. RNA concentrations were determined by using Nanodrop (Thermo Fisher Scientific). Reverse transcription was done using the kit (Applied Biosystems ref: 4,374,966). The primer for CXCR4 was provided by Applied Biosystems (Assays on demand: Mm01292123-m1). The amplification reaction was carried out with 10 ng complementary DNA samples in 96-well plates (Applied Biosystems) in a Stepone sequence detection system (Thermofisher). The studied genes were PPARγ2, AP2and LPL and the PCR mixture contained 1.5 µL of 2 mM primers and 5 µL of 2 Fast SybrGreen PCR master Mix (Applied Biosystems). Reactions were performed at 60 °C (30 s), 95 °C (3 s).

Data availability

The data supporting this article have been included as part of the Supplementary Information.

Received: 18 November 2024; Accepted: 13 March 2025
Published online: 26 March 2025

References

1. Zuk P. A. et al. Human adipose tissue is a source of multipotent stem cells. *Mol. Biol. Cell.* **13**(12), 4279–4295. https://doi.org/10.1091/mbc.e02-02-0105 (2002).
2. Aust, L. et al. Yield of human adipose-derived adult stem cells from liposuction aspirates. *Cytotherapy* **6**(1), 7–14. https://doi.org/10.1080/14653240310004539 (2004).
3. Kastrup, J. et al. Cryopreserved off-the-shelf allogeneic adipose-derived stromal cells for therapy in patients with ischemic heart disease and heart failure—A safety study. *Stem Cells Transl. Med.* **6**(11), 1963–1971. https://doi.org/10.1002/sctm.17-0040 (2017).
4. Sánchez-Guijo, F. et al. Adipose-derived mesenchymal stromal cells for the treatment of patients with severe SARS-CoV-2 pneumonia requiring mechanical ventilation. A proof of concept study. *EClinicalMedicine* **25**, 100454. https://doi.org/10.1016/j.eclinm.2020.100454 (2020).
5. Sastourné-Arrey, Q. et al. Adipose tissue is a source of regenerative cells that augment the repair of skeletal muscle after injury. *Nat. Commun.* **14**(1), 80. https://doi.org/10.1038/s41467-022-35524-7 (2023).
6. Girousse, A. et al. The release of adipose stromal cells from subcutaneous adipose tissue regulates ectopic intramuscular adipocyte deposition. *Cell Rep.* **27**(2), 323-333.e5. https://doi.org/10.1016/j.celrep.2019.03.038 (2019).
7. Fadini, G. P. et al. Circulating stem cells associate with adiposity and future metabolic deterioration in healthy subjects. *J. Clin. Endocrinol. Metab.* **100**(12), 4570–4578. https://doi.org/10.1210/jc.2015-2867 (2015).
8. Li, S. et al. Peripheral blood-derived mesenchymal stem cells: Candidate cells responsible for healing critical-sized calvarial bone defects. *Stem Cells Transl. Med.* **4**(4), 359–368. https://doi.org/10.5966/sctm.2014-0150 (2015).
9. Peng, Q., Alipour, H., Porsborg, S., Fink, T. & Zachar, V. Evolution of ASC immunophenotypical subsets during expansion in vitro. *IJMS* **21**(4), 1408. https://doi.org/10.3390/ijms21041408 (2020).
10. Sattar, N. & Gill, J. M. Type 2 diabetes as a disease of ectopic fat?. *BMC Med.* **12**(1), 123. https://doi.org/10.1186/s12916-014-0123-4 (2014).
11. Sin, A., Murthy, S. K., Revzin, A., Tompkins, R. G. & Toner, M. Enrichment using antibody-coated microfluidic chambers in shear flow: Model mixtures of human lymphocytes. *Biotechnol. Bioeng.* **91**(7), 816–826. https://doi.org/10.1002/bit.20556 (2005).
12. Castaño, N. et al. Exponential magnetophoretic gradient for the direct isolation of basophils from whole blood in a microfluidic system. *Lab Chip* **22**(9), 1690–1701. https://doi.org/10.1039/d2lc00154c (2022).
13. Di Carlo, D., Irimia, D., Tompkins, R. G. & Toner, M. Continuous inertial focusing, ordering, and separation of particles in microchannels. *Proc. Natl. Acad. Sci.* **104**(48), 18892–18897. https://doi.org/10.1073/pnas.0704958104 (2007).
14. Bhagat, A. A. S., Kuntaegowdanahalli, S. S. & Papautsky, I. Continuous particle separation in spiral microchannels using dean flows and differential migration. *Lab Chip* **8**(11), 1906–1914. https://doi.org/10.1039/B807107A (2008).
15. Hou, H. W. et al. Isolation and retrieval of circulating tumor cells using centrifugal forces. *Sci. Rep.* **3**(1), 1259. https://doi.org/10.1038/srep01259 (2013).
16. Zhao, J. et al. Separation and single-cell analysis for free gastric cancer cells in ascites and peritoneal lavages based on microfluidic chips. *eBioMedicine* **90**, 104522. https://doi.org/10.1016/j.ebiom.2023.104522 (2023).
17. Bu, J. et al. Dual-patterned immunofiltration (DIF) device for the rapid efficient negative selection of heterogeneous circulating tumor cells. *Lab Chip* **16**(24), 4759–4769. https://doi.org/10.1039/C6LC01179A (2016).
18. Hyun, K.-A., Lee, T. Y. & Jung, H.-I. Negative enrichment of circulating tumor cells using a geometrically activated surface interaction chip. *Anal. Chem.* **85**(9), 4439–4445. https://doi.org/10.1021/ac3037766 (2013).

19. Fachin, F. et al. Monolithic chip for high-throughput blood cell depletion to sort rare circulating tumor cells. *Sci. Rep.* https://doi.org/10.1038/s41598-017-11119-x (2017).
20. Kim, S. H. et al. Cancer marker-free enrichment and direct mutation detection in rare cancer cells by combining multi-property isolation and microfluidic concentration. *Lab Chip* **19**(5), 757–766. https://doi.org/10.1039/C8LC00772A (2019).
21. Zen, N. T. K. et al. Scalable mesenchymal stem cell enrichment from bone marrow aspirate using deterministic lateral displacement (DLD) microfluidic sorting. *Lab Chip* **23**(19), 4313–4323. https://doi.org/10.1039/D3LC00379E (2023).
22. Yamada, M. & Seki, M. Hydrodynamic filtration for on-chip particle concentration and classification utilizing microfluidics. *Lab Chip* **5**(11), 1233. https://doi.org/10.1039/b509386d (2005).
23. Yang, S., Ündar, A. & Zahn, J. D. A microfluidic device for continuous, real time blood plasma separation. *Lab Chip* **6**(7), 871–880. https://doi.org/10.1039/B516401J (2006).
24. Wu, Z., Willing, B., Bjerketorp, J., Jansson, J. K. & Hjort, K. Soft inertial microfluidics for high throughput separation of bacteria from human blood cells. *Lab Chip* **9**(9), 1193. https://doi.org/10.1039/b817611f (2009).
25. Stressmann, M. & Moresoli, C. Effect of pore size, shear rate, and harvest time during the constant permeate flux microfiltration of CHO cell culture supernatant. *Biotechnol. Prog.* **24**(4), 890–897. https://doi.org/10.1002/btpr.4 (2008).
26. Qin, Q., Wang, J., Cheng, Z., Cui, Z. & Li, J. Investigation of shear-force distribution in the hollow fiber membrane module based on FBG sensing technology. *Sep. Purif. Technol.* **250**, 116458. https://doi.org/10.1016/j.seppur.2019.116458 (2020).
27. Fouet, M. et al. Filter-less submicron hydrodynamic size sorting. *Lab Chip* **16**(4), 720–733. https://doi.org/10.1039/C5LC00941C (2016).
28. Gentile, P. & Garcovich, S. Concise review: Adipose-derived stem cells (ASCs) and adipocyte-secreted exosomal microRNA (A-SE-miR) modulate cancer growth and proMote wound repair. *J. Clin. Med.* **8**(6), 855. https://doi.org/10.3390/jcm8060855 (2019).
29. Ceccarelli, S., Pontecorvi, P., Anastasiadou, E., Napoli, C. & Marchese, C. Immunomodulatory effect of adipose-derived stem cells: The cutting edge of clinical application. *Front. Cell Dev. Biol.* **8**, 236. https://doi.org/10.3389/fcell.2020.00236 (2020).
30. Mahmoud, M. & Abdel-Rasheed, M. Influence of type 2 diabetes and obesity on adipose mesenchymal stem/stromal cell immunoregulation. *Cell Tissue Res.* **394**(1), 33–53. https://doi.org/10.1007/s00441-023-03801-6 (2023).
31. Zhu, S. et al. Inertial microfluidic cube for automatic and fast extraction of white blood cells from whole blood. *Lab Chip* **20**(2), 244–252. https://doi.org/10.1039/C9LC00942F (2020).
32. Abdulla, A., Liu, W., Gholamipour-Shirazi, A., Sun, J. & Ding, X. High-throughput isolation of circulating tumor cells using cascaded inertial focusing microfluidic channel. *Anal. Chem.* **90**(7), 4397–4405. https://doi.org/10.1021/acs.analchem.7b04210 (2018).
33. Nivedita, N. & Papautsky, I. Continuous separation of blood cells in spiral microfluidic devices. *Biomicrofluidics* **7**(5), 054101. https://doi.org/10.1063/1.4819275 (2013).
34. Guzniczak, E. et al. Deformability-induced lift force in spiral microchannels for cell separation. *Lab Chip* **20**(3), 614–625. https://doi.org/10.1039/C9LC01000A (2020).
35. Munaz, A., Shiddiky, M. J. A. & Nguyen, N.-T. Recent advances and current challenges in magnetophoresis based micro magnetofluidics. *Biomicrofluidics* **12**(3), 031501. https://doi.org/10.1063/1.5035388 (2018).

Acknowledgements

This work was supported by the French Research Agency ANR project ASCFINDER n° ANR-20-CE19-0010-02, Université Paul Sabatier III, the Occitanie region and MITI-CNRS. This work was partially supported by the platform of micro and nanotechnologies of the LAAS-CNRS, Member of the French network RENATECH. This project has also been labelled by the European Cancer and Rejuvenation graduate school EuCaRe. We acknowledge Elodie Riant and/or Alexia Zakaroff-Girard from the I2MC cytometry and cell sorting facility (Genotoul-TRI), member of the national infrastructure France-BioImaging supported by the French National Research Agency (ANR-10-INBS-04)

Author contributions

M.B., M.V. and performed the microfluidic experiments. M.A., A.V. and CS conducted the ASC extraction, flow cytometry experiments and data acquisition. E.T., C.S. and A.G designed the experiments and supervised the work. M.B. prepared the original draft and A.G, ET and C.S restructured and revised it. All authors participated in reviewing the manuscript.

Funding

French Research Agency (ANR) project ASC-FINDER, ANR-20-CE19-0010-02.

Declarations

Competing interests

The authors declare no competing interests.

Additional information

Supplementary Information The online version contains supplementary material available at https://doi.org/10.1038/s41598-025-94353-y.

Correspondence and requests for materials should be addressed to M.-H.B. or A.-M.G.